Deformation Texture Modelling by Mean-Field and Full-Field Approaches

Jurij J. Sidor[1,*] and Qingge Xie[2]

[1]*Eötvös Loránd University (ELTE), Faculty of Informatics, Savaria Institute of Technology, Károlyi Gáspár tér 4, Szombathely, 9700, Hungary*
[2]*Collaborative Innovation Center of Steel Technology, University of Science and Technology Beijing, Beijing, 100083, China*

*Corresponding author: E-mail: js@inf.elte.hu

Received: 16 April 2019, Revised: 05 June 2019 and Accepted: 11 June 2019

DOI: 10.5185/amlett.2019.0030
www.vbripress.com/aml

Abstract

An analysis on modeling the rolling textures in Al alloy by means of mean-field and full-field approaches is presented in the current contribution. The mean-field simulations were performed by the Taylor-type homogenization approach, called Alamel model, which takes into account a short-range interaction between the grains in a polycrystalline system. In order to account for the intra-grain deformation phenomena, the crystal elasto-visco-plastic finite-element model was employed. The method of strain path approximation on the quality of texture prediction was likewise discussed. The deformation history was calculated with different analytical approaches and a finite element model with isotropic mechanical properties, which accounted for various degree of accuracy. It was shown that the analytical approximations accoupled with the crystal plasticity model employed are capable of carrying out texture simulations close to the one performed with the crystal plasticity model with the deformation history obtained by means of the finite element model. Comparison of modelled and experimental textures as well as analysis of qualitative texture indicators suggest that an improvement in texture simulation can be achieved by considering heterogeneities of deformation flow across the thickness and taking into account the inhomogeneous nature of deformation inside each grain. Copyright © VBRI Press.

Keywords: Al alloy, texture, crystal plasticity modelling, alamel model.

Introduction

Thermo-mechanical processing (TMP) of rolled Al alloys involves both deformation and recrystallization, which are responsible for the evolution of microstructure with specific crystallographic texture [**1**]. Varying technological parameters of TMP chain accounts for different material's behavior during deep-drawing or other applications. Since the influence of technological parameters on both microstructure and texture is not entirely understood, implementation of numerical approaches is of great importance.

In Al alloys, subjected to both hot and cold rolling and afterward annealed at the temperature which induces discontinuous recrystallization, the evolution of texture has a specific pattern, characteristic for each step of thermo-mechanical processing. For instance, the texture components of cold rolled sheets are aligned along the α and β fibres [**2**], whereas the recrystallization (RX) texture is mainly characterized by the θ-fibre orientations mixed with the weaker α-fiber components (see **Fig. 1** for details). However, the hot rolled Al plate reveals both deformation and RX texture orientations since this deformation process is performed at elevated temperature [**1**].

It should be underlined that texture evolution in TMP is a continuous mesoscopic transformation, where each step has a great influence on the following one. For instance, interrupting the cold rolling by intermediate annealing has a strong effect on recrystallization texture [**3**] or materials with different hot band texture subjected to identical reduction account for diverse final annealing texture [**1, 4**]. Therefore, investigation of texture evolution during each step of TMP is of crucial importance. In this view, current contribution analyses the crystallographic texture changes in an Al alloy from the 6xxx series, which was subjected to rolling by means of various numerical techniques.

To reveal the true nature of mesoscopic transformation involved in deformation, both mean-field and full-field approaches are usually employed. The full-field models, such as crystal plasticity finite element methods (CPFEM) [**5-8**] enable investigating the behavior of a polycrystalline aggregate at both microscopic and macroscopic levels and allow examination of deformation flow at distinctive deformation rates and temperatures. The CPFEM with different crystal plasticity constitutive models [**9-11**]

were successfully employed to simulate the deformation behavior of single crystalline materials as well as polycrystalline systems. The mean-field approximations [**12-16**], treating the material as a continuum at the level of single grain, are effective approaches to simulate the behavior of polycrystalline systems, where each grain interacts with the neighborhood in a predefined way. The above-mentioned approaches were employed not only for predicting the evolution of crystallographic texture during deformation, but also for estimation of anisotropy of plastic strain ratio [**17, 1**8], which is a decisive factor for deep-drawing qualities of Al alloys. It was shown that the choice of full-field approximation and homogenization technique in the mean-field models affects the accuracy of numerical simulations [**17, 19**].

Though numerous attempts have been made to simulate the evolution of texture in rolling or other TMP step [**5-16, 19, 20**], often the computation was based on a particular crystal plasticity model accoupled with one specific approach to approximate the deformation history. In this contribution, a concise analysis of modeling the rolling texture by both full-field and mean-field approaches is presented. The major aim of this work is to reveal the distinctive features of each numerical approach and analyze the quality of simulation by comparing the computed texture with the experimentally measured counterpart. In addition, the implementation of diverse approaches will contribute to a better understanding of deformation phenomena involved in rolling. The investigation will also help in determining an efficient and reasonably accurate numerical approach, which can be implemented for texture simulation during a cold rolling process.

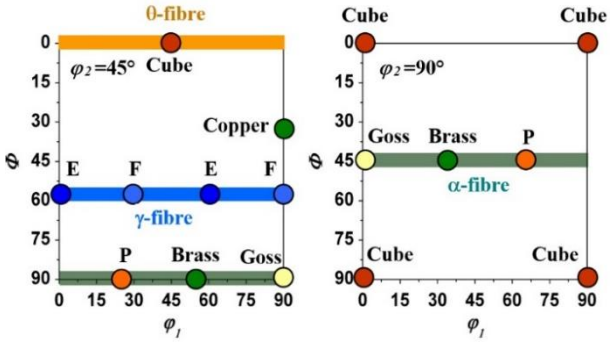

Fig. 1. Main orientations and fibres, observed in materials with face centered cubic crystal structure.

Experimental and computational procedure

Al-Mg-Si aluminum alloy from 6016 series with the initial thickness of 1.125 mm was subjected to a single pass cold rolling. The fully recrystallized material was deformed by the laboratory rolling mill with a roll diameter of 129 mm. Prior to rolling and after 17.96% thickness reduction, the through-thickness textures were measured in both materials by means of electron backscattering diffraction (EBSD). The orientation data were analyzed by the commercial OIM-TSL-8® software.

Sample preparation for EBSD examination was completed according to the standard procedure involving mechanical grinding, mechanical polishing as well as electrolytic polishing. The mechanical polishing was finished with 1 μm diamond paste while the electrolytic polishing was conducted for ~1 min at a voltage of 18V with A2 Struers® electrolyte, cooled to temperatures ranging between -5 and 0°C.

In the pre-rolling stage, the texture of the investigated material with fully recrystallized microstructure was measured at the acceleration voltage of 20kV. However, in the deformed material, to avoid overlapping of acquired pattern with ones originating from the deeper layers, the acquisition of EBSD patterns was performed at a comparatively low acceleration voltage. Application of 15kV ensured appropriate EBSD data acquisition. During EBSD measurements, the samples were 70° tilted with respect to the EBSD detector. The EBSD mapping was performed on a hexagonal scan grid in the plane perpendicular to the sample transverse direction (TD-plane) extending over the entire thickness of the investigated sample. For accurate texture evaluation, the deformed sample was scanned with a step size of 1.5 μm, while the recrystallized material was investigated with the 5 μm step.

In order to ensure a meaningful comparison between the experimentally measured and simulated textures, both orientation data were post-processed with the MTM-FHM software [**21**]. In either case, the discrete set of orientations was converted to a continuous orientation distribution function (ODF). The calculated textures are displayed in the φ_2 = const sections.

The evolution of cold rolling texture was analyzed by means of crystal elasto-visco plasticity finite element model (CEVPFEM) as well as a Taylor-type homogenization approach called advanced lamel model (Alamel) [**12**]. The texture evolution was simulated by taking into account the {111} <110> octahedral slip systems. For modeling purposes, the experimentally measured texture of pre-rolling stage was converted to a continuous ODF and afterward discretized. The experimental ODF was transformed into a set of 24000 equally weighted orientations.

In order to calculate the evolution of texture, the strain velocity gradients should be provided to the crystal plasticity (CP) model employed. First, the rolling was approximated by plane strain compression (PSC), whereas, with the aim of more accurate approximation of strain heterogeneity through the thickness, two-dimensional finite element (FEM) simulations, flow-line modeling (FLM) [**22**] and calculations by the simple geometric model (SGM) [**19**] were performed. In the SGM, FLM and FEM calculations, the material, subjected to deformation, is considered as plastic and isotropic. In the finite element

modelling, material's hardening was described with the stress-strain curve fitted by piecewise linear segments and the rolls were considered as fully rigid objects, whereas in both the SGM and FLM the strain hardening effect was neglected. The following material parameters were used in FEM simulations for isotropic aluminum matrix: Young's Modulus E = 68.9 GPa, Poisson's ratio ν = 0.33 and the yield strength σ_y = 80 MPa. In the SGM, FEM and FLM simulations, the strain rate components were calculated for the surface, 1/5th, 2/5th, 3/5th, 4/5th of the half thickness and mid-thickness plane. The extracted outputs were used as an input for crystal plasticity (Alamel) calculation of through-thickness textures.

In the full-field CEVPFEM simulations, in total 23.9×10^3 grains (crystals) were represented by 10^6 elements, while each grain could be represented by up to 100 elements to capture the heterogeneous nature of deformation within a particular crystal. It should be mentioned that generation of virtual microstructure with a particular texture is a complex procedure, consisting of numerous iteration steps. This process often accompanied by a loss of some orientations, since it is not always possible to assign a certain number of orientations to a predefined number of grains. In the current case, 100 orientations out of 24000 were vanished during the iterative microstructure generation. The orientations in the generated microstructure are represented by float numbers (Euler angles) following Bunge's convention. The boundary condition on key nodes in the CEVPFEM was PSC.

Results obtained by CEVPFEM, PSC-CP, FEM-CP, FLM-CP, and SGM-CP simulations were compared with the experimentally measured counterpart.

Material's flow modelling during cold rolling

Geometrical approaches

Plane strain compression approximation reflects to a large extent the change of material's shape in rolling and owing to a simplicity this analysis is often used in texture simulation. In wet rolling (well-lubricated surfaces), PSC is justified since the ratio between the compressive (L_{33}=-L_{11}) and shear (L_{ij} ($i\neq j$)) components in the strain velocity gradient tensor is great. In this approximation, L_{ij}=0 if $i\neq j$, while $|L_{ij}|>0$ if $i=j$, however, L_{22} is assumed to be 0. Here, directions 1, 2 and 3 correspond to rolling (RD), transverse (TD) and normal (ND) directions, respectively. In its simplest form, the L_{11} component is calculated as:

$$L_{11} = \dot{\varepsilon}_{11} \approx \frac{1}{\Delta t} ln\left(\frac{h_i}{h_f}\right) \quad (1)$$

where h_i and h_f are the initial and final thickness, and Δt is the time increment.

It should be noted that PSC corresponds to a simulation with a constant strain rate and rate dependent behavior is neglected in the current analysis.

Recently, a simple geometric model (SGM) was developed [**19**] for rolling, enabling calculation of strain velocity gradient tensor components for various thickness layers (p):

$$L^p = \begin{bmatrix} 0.5\pi\dot{\varepsilon}_{11}\, sin(\pi\tau) & 0 & m^{-1}\pi\dot{\gamma}^p\, sin(2\pi\tau) \\ 0 & 0 & 0 \\ -m\pi\dot{\gamma}^p\, sin(2\pi\tau) & 0 & -0.5\pi\dot{\varepsilon}_{11}\, sin(\pi\tau) \end{bmatrix} \quad (2)$$

with:

$$\dot{\gamma}^p = \dot{\gamma}\, exp\left(\frac{s-1}{s}\right) \quad (3)$$

$$\dot{\gamma} = \frac{\Delta h}{\Delta t(R\Delta h-(0.5\Delta h)^2)^{0.5}} \quad (4)$$

where, R is a roll radius, Δh = (h_i - h_f), $\tau(0\leq\tau\leq1)$ is a ratio of the instantaneous normal strain to its maximum value, m is a fitting parameter (m>0), the superscript p indicates the position of a given layer with respect to the surface of a rolled sheet and s varies between 0 and 1: s=1 for the surface, whereas in the mid-thickness plane $s \rightarrow 0$.

By way of contrast to PSC, the SGM (Eq. 2) partially accounts for the effect of roll gap geometry, strain heterogeneities across the thickness, whereas m reflects the effect of friction.

FEM

To account for the deformation flow across the thickness, finite element simulations were carried out for an isotropic material, by assuming a constant Coulomb friction coefficient μ. In the current FEM simulation, which corresponds to the formulation and numerical implementation of the von Mises criterion, the value of μ was slightly exceeding the minimum friction coefficient (μ_{min}) necessary for rolling ($\mu=1.1\mu_{min}$) inasmuch as both sheet and rolls were well-lubricated. The μ_{min} can be computed by the following expression [**23**]:

$$\mu_{min} = \frac{1}{2}\sqrt{\frac{h_f}{R}}\frac{ln\left(\frac{h_i}{h_f}\right)+\frac{1}{4}\sqrt{\frac{h_i-h_f}{R}}}{tan^{-1}\sqrt{\frac{h_i}{h_f}-1}} \quad (5)$$

To simulate the evolution of texture, the deformation history in a form of L, for various through-thickness layers, was fed to the Alamel model.

FLM

Flow-line models [**22, 24, 25**] are analytical approaches, which are capable of describing the deformation flow under given boundary conditions for a particular process. In the FLM employed, the detailed mathematical description of which is described elsewhere [**22**], a kinematically admissible displacement velocity field fulfills the following boundary conditions: (a) the entrance and the exit

velocity of a rolled sheet is even across the thickness, (b) the incompressibility condition is fulfilled at all points, (c) material's flow occurs along the prescribed streamlines in the middle and surface of the plate, however, a small deviation from the predefined stream-lines for other layers is allowed, (d) at the surface, the velocity field is prescribed by means of model parameter α, which guarantees a difference between velocities of surface and mid-thickness layers and might be linked to friction coefficient, (e) the variation of the velocity across the thickness is conditioned by the *n*-th power law, (f) the model does not allow any displacement in TD, i.e. $L_{22}=0$. This two-dimensional FLM approach allows efficient calculation of velocity gradient history, evolved across the thickness of a rolled sheet. Results of FLM simulations are compared with the ones obtained by the SGM and FEM.

Crystal elasto-visco-plastic finite-element modelling

The full-field crystal elasto-visco-plastic finite-element (CEVPFE) [**8**] simulation has been implemented for texture simulation. This computational approach was already employed for both successful prediction of residual lattice strain in an IF steel [**26**] and simulation of anisotropic behavior of AA6016 Al alloy [**27**].

In the current crystal elasto-visco-plastic constitutive relation, we follow the integration procedure described in detail by Gorti and Thomas [8]. The deformation gradient **F** is divided into plastic deformation ($\mathbf{F^p}$), the lattice rotation ($\mathbf{R^*}$) and the elastic stretch $\mathbf{F^e}$:

$$\mathrm{F} = \mathrm{F^e R^* F^p} = \mathrm{F^* F^p} \tag{6}$$

The velocity gradient L corresponding to F is calculated as:

$$\mathrm{L} = \dot{\mathrm{F}}\mathrm{F}^{-1} = \dot{\mathrm{F}}^*\mathrm{F}^{*-1} + \mathrm{F}^*\dot{\mathrm{F}}^{\mathrm{p}}\mathrm{F}^{\mathrm{p}-1}\mathrm{F}^{*-1} = \mathrm{L}^* + \mathrm{L}^{\mathrm{p}} \tag{7}$$

In this model, we set the configuration before and after a strain increment as B_0 and B, respectively. In addition, two intermediate configurations are introduced: one is right after $\mathbf{F^p}$, indicated as $\widetilde{\mathrm{B}}$, and the other one is right after applying $\mathbf{R^*}$, indicated as $\overline{\mathbf{B}}$. For each strain increment, the integration equation is written for the intermediate configuration $\widetilde{\mathrm{B}}$. Therefore, for the $\widetilde{\mathrm{B}}$ -type configuration, the grain orientation initially does not rotate and the critical resolved shear stress (CRSS) is assumed to be equal to the one corresponding to the beginning of current strain increment. In this view, we define the $\mathbf{L^p}$ tensor as following:

$$\mathbf{L^p} = \mathbf{F^* \tilde{L}^p F^{*-1}} \tag{8}$$

Here $\mathbf{\tilde{L}^p}$ is the velocity gradient corresponding to $\widetilde{\mathrm{B}}$ and it can also be expressed in the following form:

$$\mathbf{\tilde{L}^p} = \sum_{\alpha=1}^{N} \dot{\gamma}^{\alpha} \widetilde{\boldsymbol{b}}^{\alpha} \otimes \widetilde{\boldsymbol{n}}^{\alpha} \tag{9}$$

where $\widetilde{\boldsymbol{b}}^{\alpha}$ and $\widetilde{\boldsymbol{n}}^{\alpha}$ are the slip direction and slip plane normal vectors for the slip system α, which runs from 1 to N.

It should be taken into account that:

$$\widetilde{\boldsymbol{b}}^{\alpha} = \boldsymbol{b}_0^{\alpha} \widetilde{\boldsymbol{n}}^{\alpha} = \boldsymbol{n}_0^{\alpha} \tag{10}$$

According to equations 8-10, the $\mathbf{L}^p$ can be rewritten as:

$$\mathbf{L^p} = \sum_{\alpha=1}^{N} \dot{\gamma}^{\alpha} \mathbf{F}^* \tilde{b}^{\alpha} \otimes \tilde{n}^{\alpha} \mathbf{F}^{*-1} = \sum_{\alpha=1}^{N} \dot{\gamma}^{\alpha} \boldsymbol{b}^{\alpha} \otimes \boldsymbol{n}^{\alpha} \tag{11}$$

By employing eqs.7 and 11, the following expression is obtained:

$$\dot{\mathbf{F}}^* = \mathbf{L}\mathbf{F}^* - \mathbf{F}^* \sum_{\alpha=1}^{N} \dot{\gamma}^{\alpha} \widetilde{\boldsymbol{b}}^{\alpha} \otimes \widetilde{\boldsymbol{n}}^{\alpha} \tag{12}$$

where, the slip rate of each slip system adopts the visco-plastic law:

$$\dot{\gamma}^{\alpha} = \dot{\gamma}_0 \left| \frac{\tau^{\alpha}}{\tau_c^{\alpha}} \right|^n \tag{13}$$

Equation 12 was implemented to calculate the $\mathbf{F}^*$ tensor for an intermediate configuration $\widetilde{\mathrm{B}}$, according to the procedure given in [**8**]. The deformation gradient $\mathbf{F}^*$is a key tensor in the current model, since both the second Piola-Kirchoff stress tensor and the Green strain tensor are related to it. The former follows the Hooke's law and it is used to calculate the Cauchy stress. On the other hand, the small elastic strain assumption, as introduced in Ref. [**8**], was employed in the finite-element integration procedure. The details of the computational algorithm are described elsewhere [**28, 29**]. The Voce-type law [**30**] was implemented to take into account the strain hardening phenomena, where the evolution of the threshold stress τ_a is correlated to the accumulated shear strain Γ:

$$\tau_a = \tau_0 + (\tau_1 + \Gamma\theta_1)(1 - \exp(-\Gamma\theta_0/\tau_1)) \tag{14}$$

where τ_0, θ_0, θ_1 and $(\tau_0 + \tau_1)$ are: the initial threshold stress, the initial hardening rate, the asymptotic hardening rate and the back-extrapolated threshold stress, respectively.

In the current CP simulations, the following Voce parameters were used: τ_0 = 26.6MPa, τ_1 = 31.5MPa, θ_0 = 27.5 MPa, θ_1 = 0.1 MPa.

To approximate the PSC, the following boundary conditions were imposed in the CEVPFEM: the velocity in the TD of all nodes in outside surface in the two TD planes are set to zero; the velocities in ND of all nodes in the bottom are likewise set zero; the velocity in the ND of all nodes in the top surface are enforced to meet the PSC. The velocity in the RD of all nodes in the outside surface of one end of the model (a symmetry plane assumed in the model) is set to zero.

Results and discussion

Evolution of the crystallographic texture through the thickness of the investigated material is shown in **Fig. 2a** and **Fig. 2b**. Preceding the deformation, the ODF consists of components such as a strong cube ({100}<001>) and weakly developed Goss ({110}<001>), which are characteristic for the fully

recrystallized state. After 18% rolling, the recrystallization texture (**Fig. 2a**) transforms to the new one (**Fig. 2b**), composed of β-fibre orientations [**2**] and retained RX texture components. **Fig. 2b** shows that the intensity of the cube texture has not declined significantly, pointing towards the stability of this orientation in rolling. The simulation of texture evolution, presented in **Fig. 2c**, was performed for seven equally distanced layers (from the surface to mid-thickness) with characteristic pre-rolling texture for each separate layer. The average through-thickness texture was calculated by merging the individual ODFs. The simulation of texture evolution presented in **Fig. 2c** was performed by the Alamel model, wherein a homogeneous PSC condition was assumed. In this calculation, both the role of the roll gap geometry and corresponding strain heterogeneity across the thickness are neglected. The ODF of **Fig. 2d** was calculated by the CEVPFEM, and here the strain heterogeneity through the thickness is totally up to the microstructure and texture heterogeneity. The PSC boundary condition provides reasonable texture prediction in either case, however, some quantitative discrepancies can be observed between the modelled and experimental counterparts. The accuracy of particular texture simulation can be estimated by the texture index difference *TID*, observed between the experimental $f_{exp}(g)$ and simulated $f_{sim}(g)$ ODFs, which tends to rise with the increase of differences between the compared ODFs:

$$TID = \int \left[f_{exp}(g) - f_{sim}(g) \right]^2 dg \qquad (15)$$

Comparison of texture quantitative indicators (*TIDs*), calculated for **Figs. 2c** and **d**, tends to enhance the advantage of the full-field modelling over the mean-field approach. The Alamel model provides the *TID* of 0.12, whereas the CEVPFEM employed ensures a two-times lower value (*TID*=0.06). The principal difference between the two approaches is that in the Taylor-type homogenization approaches such as the Alamel model, the grain prior and after the deformation remains a single crystal with no in-grain orientation spread, while crystal plasticity finite element models serve to produce a pronounced misoriented structures within each grain, as it is shown in **Fig. 3**. Additionally, the CEVPFEM accounts for all grain-interaction ranges. The modelled microstructure of **Fig. 3** is fully versed in the wide range of experimental evidences and, therefore, better represents the nature of a deformed state. The main advantage of the mean-field approach employed (Alamel) is that the texture simulation can be completed within a time-frame of several minutes (on a personal computer (PC) with 16 GB of RAM memory and CPU running at a frequency of 2.6 GHz with a single thread), while crystal plasticity full-field computation of 18% reduction requires a couple of days (on the PC with 512 GB of RAM memory and CPU running at a frequency of 2.6 GHz with 156 threads).

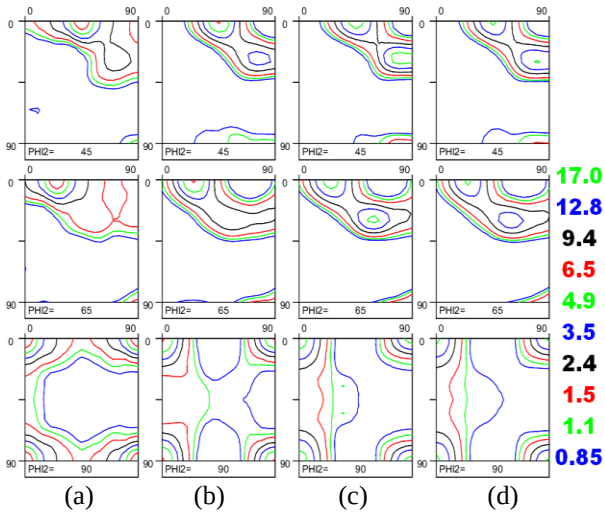

Fig. 2. Texture evolution in the investigated material: a) ODF prior to rolling; b) experimentally measured deformation texture; c) modeled texture with the Alamel model, assuming plane strain compression, *TID*=0.12; d) result of CEVPFEM calculation, assuming PSC, *TID*=0.06.

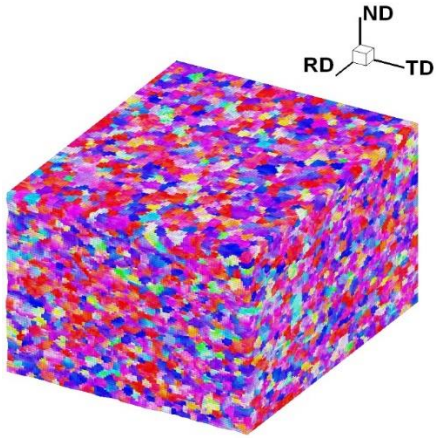

Fig. 3. Evolution of microstructure, as predicted by the CEVPFEM employed. Prior to deformation, all grains were perfect crystals. The color in the model is decoded by the ND inverse pole figure as normally used for the EBSD data representation.

In order to account for the effect of friction in rolling, which induces deformation heterogeneity through the thickness of a sheet, the strain history for crystal plasticity simulations was calculated by the SGM, FLM and FEM, respectively. Since the implementation of continuously changing strain path in CEVPFEM is intricate and the computation is time demanding, this approach was excluded from further texture simulations. Feeding the deformation history, computed by various approaches, to the CP model employed (Alamel) gives rise to reasonably accurate texture simulations. Results of texture prediction by combining Alamel model with the SGM, FEM and FLM are presented in **Fig. 4**. The quality of texture simulation, expressed in term of *TID*, has significantly improved, compared to the case when rolling was approximated by PSC (see **Fig. 2** and **Fig. 4**). Independently of the strain mode approximation employed, the calculated ODF textures manifest low *TIDs*: *TID* (SGM) = 0.06, *TID* (FEM) = 0.07 and *TID*

(FLM) = 0.06. The common feature of all models employed for strain path calculation is that all these approaches account for both strain path change during the deformation and strain mode heterogeneity across the thickness.

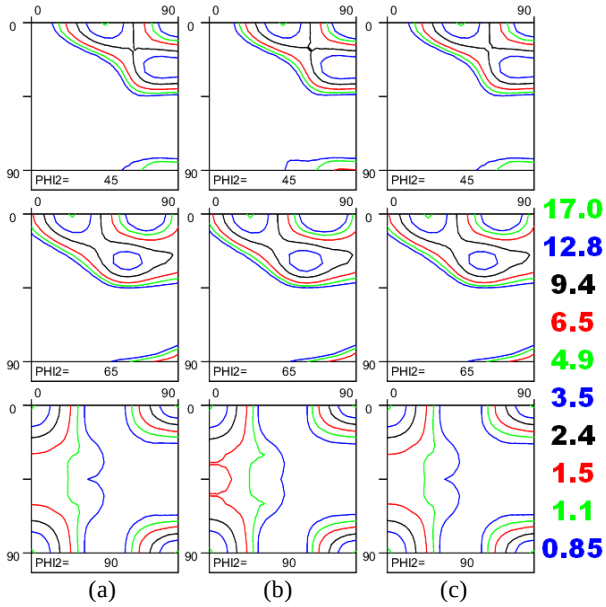

Fig. 4. Texture evolution in the investigated material modelled texture with the Alamel model: a) the deformation history is calculated by the SGM (equation 2), *TID*=0.06; b) stain path is calculated by FEM, *TID*=0.07; c) stain mode is computed by the FLM, *TID*=0.06.

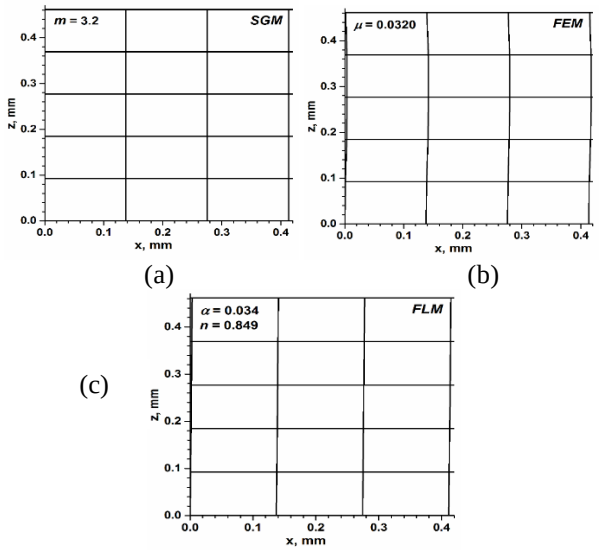

Fig. 5. Distortion of initially rectangular elements across the half-thickness after 18% reduction, as predicted by various models: a) simple geometric model (the fitting parameter *m*=3.2); b) FEM (μ=0.032); c) FLM. The fitting parameters (a and c) and friction coefficient used (b) are displayed on the corresponding figures.

Fig. 5 shows the distortion of initially rectangular elements across the half-thickness calculated by the approaches employed. The heterogeneity of displacement fields across the thickness is partially taken into account in the SGM (equation 2), wherein the balance between the geometric and friction-induced shear components is ensured by the fitting parameter *m*. The approximate value of *m* might be computed as $m = 100\mu_{min}$ (Eq.5), however, in the current simulation the value of *m* was set to 3.2 ($m = 110\mu_{min}$), implying that rolling was performed with μ, which slightly exceeds the friction coefficient (μ_{min}), which is necessary for rolling ($\mu = 1.1\mu_{min}$). Although the grid distortions produced by the SGM (Fig.5a) and PSC (where the contribution of both shear and strain heterogeneity are neglected) are identical, the strain paths in these approximations follow diverse evolutionary patterns and therefore the simulated textures reveal quantitative differences (see **Figs. 2c** and **4a**). The deformation patterns calculated by the FEM and FLM are shown in **Fig. 5b** and **Fig. 5c**, respectively. In the FLM used, a combination of model parameters (α and *n*) was set as to resemble the deformation pattern of **Fig. 5b**, calculated by FEM with $\mu = 1.1\mu_{min} = 0.032$. The correlation between the α, *n* and friction coefficient is not straight forward, however, the dependence of the FLM model parameters over the μ might be determined for a given rolling mill, by performing series of FEM simulations with different μ and fitting the α, *n* in the FLM to ensure the minimal deviation between the corresponding patterns. For instance, **Fig. 6** shows the correlation between the fitting parameters (α and *n*) and friction coefficient for various straining levels, accomplished with the rolling mill with a roll diameter of 129 mm. The model parameters α = 0.034 and *n* = 0.849 tend to produce a deformation pattern, comparable to one computed by FEM with μ = 0.0435. Analyzing the texture quantitative indicators obtained (**Fig. 4**), it turned out that computationally efficient analytical approaches (SGM or FLM) combined with the Alamel model can provide texture calculation as accurate as one obtained with the deformation history calculated by means of FEM.

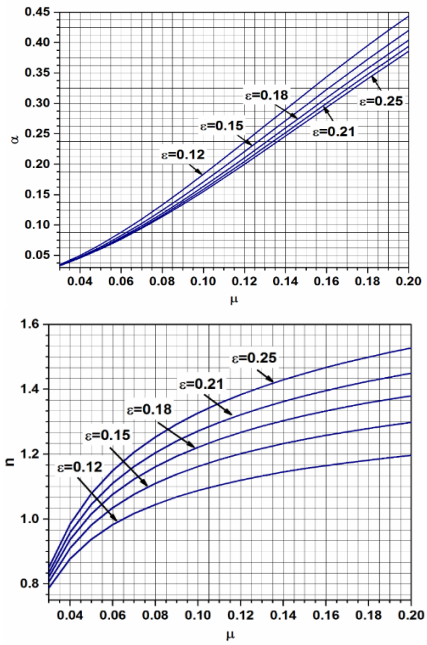

Fig. 6. Correlation between fitting parameters (α and n), employed in FLM, and friction coefficient μ.

Fig. 7 reveals the distribution of both experimentally measured and simulated orientation intensities along the α, β and θ– fibres. Both α, and θ– fibres are shown in **Fig. 1**, whereas the reference components of the β-fiber can be computed by [**2**]:

$$\{h,\quad 1,\quad h+1\}\left\langle \frac{h(h+1)}{3/4-h},\quad \frac{2h(h+1)}{1/2-h},\quad \frac{h^2}{h-3/4}+\frac{2h}{h-1/2}\right\rangle \qquad (16)$$

Substituting various values of h to equation 16 provides a spectrum of orientations along the β-fiber: for h = 1 - {112}⟨111⟩, for h = 1.5 - {325}⟨10 15 12⟩, for h = 2 - {213}⟨9 15 11⟩, for h = 3 - {314}⟨5 9 6⟩ and when h becomes infinitely large the formula reproduces {101}⟨121⟩ component.

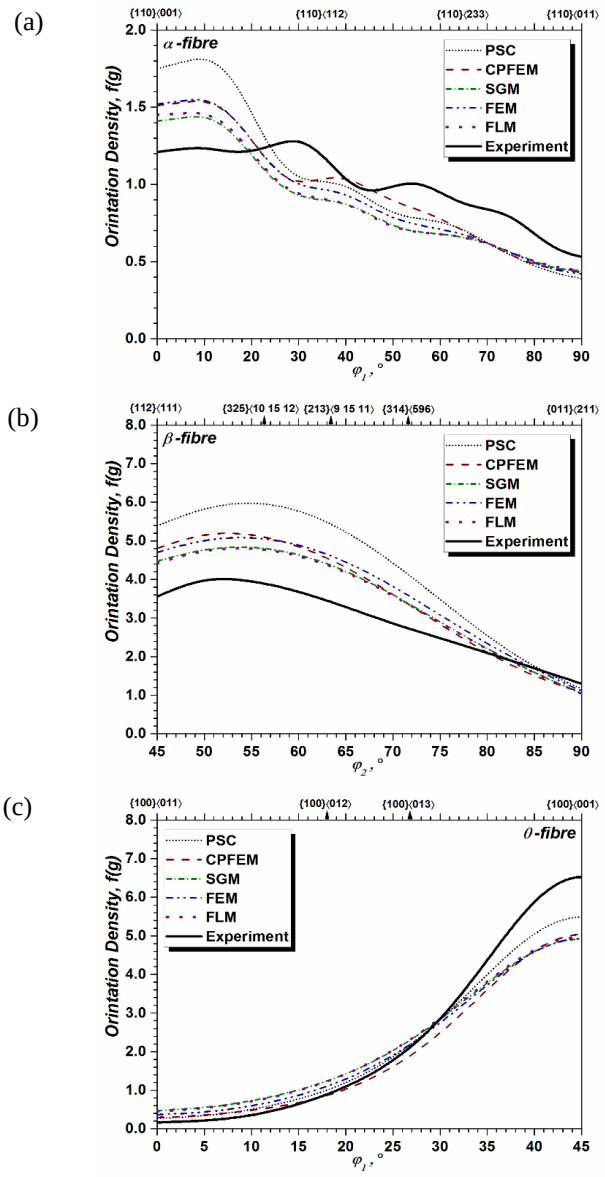

Fig. 7. Distribution of orientation intensities along texture fibres: (a) α– fibre, φ_2=90° and Φ=90°; (b) β–fibre; (c) θ–fibre, φ_2=45° and Φ=0°. In the mean-field simulations, the strain path for the crystal plasticity code employed (Alamel) was approximated by various models, such as PSC, SGM, FEM and FLM (see text for details). In the CEVPFEM, the imposed boundary condition for the key nodes was PSC.

Analyzing the distribution of orientation intensities in **Figs. 7 a-c**, it can be noticed that independently of the strain history approximation (PSC, SGM, FEM or FLM), implementation of the Alamel model provides a qualitatively reasonable texture prediction. In the case of mean-field modelling, PSC seems to be less successful in term of *TID* as compared to the SGM, FEM or FLM, which reveal comparable evolutionary patterns. Combination of PSC with the Alamel model produces sharper textures with respect to the experimental one since this strain mode neglects the strain heterogeneity across the thickness and this scenario does not seem to be actual during real deformation. Even though PSC disregards many phenomena involved in rolling, significant improvement in texture prediction is observed when the CEVPFEM is employed. In the case of CEVPFEM, the improvement of quality of simulation is attributed to the capability of the full-field model in capturing the microstructure heterogeneity through the thickness even if the PSC is assumed. It should be underlined that the PSC boundary condition is imposed on the key nodes and the deformation of other nodes are determined by the microstructure heterogeneity and the grain interactions. Results of orientation distribution presented in Figs. 7 a-c enhance the importance of (i) strain heterogeneity through the thickness and (ii) inhomogeneous deformation on a single grain level in texture simulation.

Conclusions

In the case when rolling is approximated by plane strain compression, comparison of texture quantitative indicators clearly shows the advantage of full-field modelling over the implementation of mean-field approach. The improvement is achieved because the through-thickness heterogeneity can be captured by the full-field model even if the PSC boundary condition is imposed on the key nodes. Crystal plasticity finite element model is capable of revealing pronounced misoriented structures within each grain, which is typically observed in the rolled polycrystalline aggregate.

Employing analytical models, which take into account heterogeneity of strain evolution across the thickness of a rolled sheet, tends to improve the quality of texture simulations performed by means of mean-field models. Results of texture calculations demonstrate that both a simple geometric approach and the flow line model employed in combination with the CP model, which considers grain-to-grain interaction, is capable of providing texture prediction comparable to one simulated with the strain path obtained from the finite element model.

Results of simulations suggest that significant improvement in texture simulations can be achieved by considering heterogeneous deformation flow through the thickness of a rolled sheet as well as heterogeneous nature of deformation on a single grain level.

It is reasonable to consider the practical implementation of analytical approaches since they ensure computationally efficient and quantitatively accurate texture prediction.

Acknowledgments

The financial support of EFOP-3.6.1-16-2016-00018 project: "Improving the role of research+development+innovation in higher education through institutional developments assisting intelligent specialization in Sopron and Szombathely" is gratefully acknowledged. The work was partially supported by OTKA project (identifier: 119566): "Modelling and complex experimental evaluation of texture dependent solid phase reaction in metallic systems".

References

1. Engler, O.; Hirsch, J.; *Mater. Sci. Eng. A*, **2002,** *336*, 249.
2. Sidor, J. J.; Kestens, L. A. I.; *Scripta Mater.*, **2013**, *68*, 273.
3. Bennett, T. A.; Sidor, J.; Petrov, R. H.; Kestens, L.A.I.; Adv. Eng. Mater., **2010**, *12*, 1018.
4. Sidor, J.; Petrov, R.; Kestens, L.A.I.; *Adv. Eng. Mater.*, **2011**, *13*, 1.
5. Delannay, L.; Jacques, P. J.; Kalidindi, S. R.; *Int. J. Plast.*, **2006**, *22*, 1879.
6. Dawson, P. R.; Boyce, D. E.; Rogge, R.; Com. Model. Eng. Sc., **2005**, *10***,** 123.
7. Lebensohn, R. A.; Kanjarla, A. K.; Eisenlohr, P.; *Int. J. Plast.*, **2012**, *32–33*, 59.
8. Gorti, S.; Thomas, Z.; *J. Mech. Phys. Solids*, **1999,** *47*, 1219.
9. Khan, A. S.; Liu, J.; Yoon, J. W.; Nambori R.; *Int. J. Plast.*, **2015**, *67*, 39.
10. Adzima, F.; Balan, T.; Manach, P.Y.; Bonnet, N.; Tabourot, L.; *Int. J. Plast.*, **2017**, *94*, 171.
11. Alankar, A.; Mastorakos, I. N.; Field, D. P.; *Acta Mater.*, **2009**, *57*, 5936.
12. Van Houtte, P.; Kanjarla, A. K.; Van Bael, A.; Seefeldt, M., Delannay, L.; *European J. Mech. A/Solids*, **2006**, *25*, 634.
13. Mánik, T.; Holmedal, B.; *Mater. Sci. Eng. A*, **2013**, 580, 349.
14. Zhang, K.; Holmedal, B.; Mánik, T.; Saai, A.; *Int. J. Plast.*, **2019**, *114*, 144.
15. Lebensohn, R. A.; Tomé, C. N.; *Acta Metal. Mater.*, **1993**, *41*,2611.
16. Xie, Q.; Van Bael, A.; Sidor, J.;Moerman, J.; Van Houtte, P.; *Acta Mater.*, **2014**, *69*, 175.
17. Sidor, J.; Petrov, R.; Xie, Q.; Van Houtte, P.; Kestens, L. A. I.; *Mater. Sc. Techn.*, **2017**, *33*, 667.
18. Xie, Q.; Eyckens, P.; Vegter, H.; Moerman, J.; Van Bael, A.; Van Houtte, P.; *Mater. Sci. Eng. A*, **2013**, *581*, 66.
19. Sidor, J. J.; Model. Sim. Mater. Sc. Eng., **2018,** *26*, 085011.
20. Engler, O.; Crumbach, M.; Li, S.; *Acta Mater.*, **2005**, *53*, 2241.
21. Van Houtte, P.; MTM-FHM Software 2nd Ed., MTM-KU Leuven, **1995**, 20.
22. Decroos, K.; Sidor, J.; Seefeldt, M.; *Met. Mater. Trans. A*, **2014**, *45*, 948.
23. Avitzur, B.; *Int. J. Mach. Tool. Des. Res.*, **1980**, *20*, 197.
24. Zhang, S. H.; Zhao, D. W.; Gao, C.; *Int. J. Mech. Sc.*, **2012**, *57*, 74.
25. Dogruoglu, A. N.; *J. Mater. Proc. Techn.*, **2001**, *110*, 287.
26. Xie, Q.; Gorti, S.; Sidor, J. J.; An, Y. G.; Wang, Y. D.; Lian, J.; Lan, H.; An, K.; *Steel Res. Int.*, **2018**, *89*, 1700408.
27. Xie, Q.; Van Bael, A.; An, Y.; Lian, J.; Sidor, J. J.; *Mat. Sci. Eng. A*, **2018**, *721*, 154.
28. Marin, E. B.; Dawson, P. R.; *Comput. Meth. Appl. Mech. Eng.*, **1998**, *132*, 1.
29. Gorti, S.; Balasubramaniam, R.; *Mat. Sci. Eng. A*, **2008**, *494*, 92.
30. Tomé, C. N.; Canova, G. R.; Kocks, U. F.; Christodoulou, N.; Jonas, J. J.; *Acta Metall.*, **1984**, *32*, 1637.

